Article

Monolithic Micro Light-Emitting Diode/Metal Oxide Nanowire Gas Sensor with Microwatt-Level Power Consumption

Incheol Cho, Young Chul Sim, Minkyu Cho, Yong-Hoon Cho,* and Inkyu Park*

Cite This: *ACS Sens.* 2020, 5, 563−570

Read Online

ACCESS | 📊 Metrics & More | 📰 Article Recommendations | 🆂🅸 Supporting Information

ABSTRACT: High-performance, monolithic photoactivated gas sensors based on the integration of gas-sensitive semiconductor metal oxide nanowires on micro light-emitting diodes (μLEDs) are introduced. The μLEDs showed improved irradiance and energy conversion efficiency (i.e., external quantum efficiency, EQE), as the size of LEDs was reduced from 200×200 μm^2 (irradiance of 46.5 W/cm^2 and EQE of 4%) to 30×30 μm^2 (irradiance of 822.4 W/cm^2 and EQE of 9%). Gas-sensitive zinc oxide (ZnO) nanowires were directly synthesized on top of the μLED through a hydrothermal reaction. The direct contact between the sensing component and μLED sensor platform leads to high light coupling efficiency, minimizing power consumption of the sensor. Furthermore, the sensing performance (i.e., sensitivity) at optimal operating power was improved as the LED size was reduced. The smallest fabricated gas sensor (active area = 30×30 μm^2) showed excellent NO_2 sensitivity ($\Delta R/R_0 = 605\%$ to 1 ppm NO_2) at the optimal operating power ($\sim$184 μW). In addition, the sensor showed a low limit of detection ($\sim$14.9 ppb) and robustness to high humidity conditions, which demonstrate its potential for practical applications in mobile internet of things (IoT) devices.

KEYWORDS: gas sensor, micro LED, photoactivation, metal oxide nanowire, low power sensor
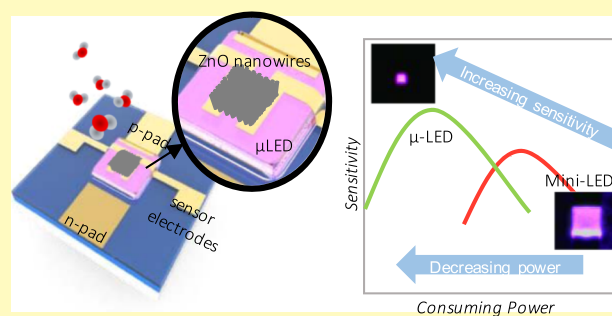
Mobile gas monitoring technology has a great potential to realize smart factory, personal health monitoring, and safety assurance from various chemical disasters and atmospheric pollution in the future internet of things (IoT) era. Among various types of gas sensors, semiconductor metal oxide (SMO) gas sensors have received much attention for the mobile gas monitoring systems because of their high sensitivity, compact size, simplicity of measurement, and low cost.[1−3] SMO gas sensors are generally activated by high-temperature heating above 200 °C for higher sensitivity, faster response speed, and complete recovery. However, the heating approach had challenges to apply on battery-driven IoT devices because of its high power consumption. So far, many studies have shown advances in lowering the operating power by means of miniaturization and thermal isolation through freestanding micro-/nanostructures (e.g., a few milliwatts with microheaters,[4−10] or hundreds of microwatts with nano-heaters[11,12]). However, the freestanding structures of those micro/nanoscale heaters make the fabrication process much more complicated and expensive. In addition, high-temperature heating may cause long-term instability, induced by thermal stress or thermal degradation of sensing nanomaterials and heating platforms.[13]

On the other hand, photoactivation allows the detection of toxic gases at room temperature and to avoid thermal damages in the gas sensor platform. It was reported that photon irradiation can increase the sensitivity by increasing the number of electron−hole pairs on the surface of SMO, which causes more adsorption of gas molecules, and by promoting the redox reactions of gas molecules on the surface.[14,15] Most research about photoactivated gas sensors has focused on novel photocatalytic materials, nanostructures, and composites. Several SMOs such as zinc oxide (ZnO), titanium oxide (TiO_2), tin oxide (SnO_2), indium oxide (In_2O_3), and their composites were widely studied as photoactivated materials, and optimal operating conditions (e.g., wavelength, irradiant power, and doping state) for activation were well established for each material.[14] However, they typically utilized high-power external light sources such as xenon lamps or prepackaged light-emitting diodes (LEDs).[16] This causes inefficient photon energy transfer, resulting in the high electrical power consumption. On the other hand, monolithic photoactivated gas sensor devices combined with a low power light source have been rarely developed.

Following several attempts to combine the light sources such as commercial LEDs or optical fibers into the sensor device,[17−19] Markiewicz et al. proposed a photoactivated

NO$_2$ gas sensor directly mounted onto a blue LED.[20,21] They suggested that monolithic integration can dramatically increase the transfer efficiency of the photon through analytic calculations and experiments. Despite this progress, there still remain many challenges, such as further miniaturization, in-depth investigation of the size dependence of sensing performance, and modulation of the activation wavelength.

Micro LED (μLED), which is commonly defined as the LED with the size less than 100×100 μm^2, is an emerging technology for future display, light communications, and biomedical applications because of its high luminous efficiency, portability, excellent stability, and fast response.[22−26] Herein, we report monolithically integrated photoactivated gas sensors combined with μLED platforms (μLP) for the first time. Gallium nitride (GaN)-based μLPs were successfully fabricated via standard microfabrication processes, which promises an industrial-grade throughput. The peak wavelength of μLPs is the near-UV region (λ_{peak} = 390 nm) to match with the absorption band of ZnO nanowires as a sensing material for efficient energy transfer. To investigate the size-dependent sensor performances, LPs with various sizes [30×30 (30-μLP), 50×50 (50-μLP), 100×100 (100-LP), and 200×200 (200-LP) μm^2] were fabricated. Here, it should be noted that the LPs smaller than 100×100 μm^2 were particularly named μLPs. An electroluminescence measurement was conducted to compare the irradiance and the energy conversion efficiency of fabricated LPs with different sizes. Then, gas-sensitive ZnO nanowires were directly synthesized on top of the fabricated μLPs through hydrothermal synthesis. Nitrogen dioxide (NO$_2$) gas, which is a representative oxidizing gas, was used to test the sensing performances of fabricated sensors. We could conclude that the size reduction of LP greatly improves the sensor performance and the power efficiency. The μLP-based photoactivated gas sensor achieved ultralow power consumption ($\sim$184 μW) with a good sensing performance. In addition, lower limit of detection (LOD) ($\sim$15 ppb) and robustness to humidity interference were experimentally demonstrated for practical applications.

■ RESULTS AND DISCUSSION

Figure 1a schematically presents the proposed μLP-based photoactivated gas sensor. It has two p−n contact electrodes for operating the LED and two interdigitated or parallel electrodes for measuring the gas sensing signal. The peak emission wavelength of the LP was 390 nm. LPs were designed to have different emitting areas of 30×30 (30-μLP), 50×50 (50-μLP), 100×100 (100-LP), and 200×200 (200-LP) μm^2 to investigate the LED size dependence of power efficiency and sensing performance. Figure 1b describes the cross-sectional layer structure of the monolithic photoactivated sensor based on gallium nitride (GaN) μLP. On top of the p-GaN, 200 nm-thick indium tin oxide (ITO) was used for the Ohmic contact with the p-GaN layer. Silicon dioxide (SiO2) (500 nm thick) were deposited by chemical vapor deposition (CVD) in between the LED and the sensor electrodes for electrical insulation. Hydrothermally grown zinc oxide (ZnO) nanowires were chosen as the sensing material because of their excellent gas diffusivity, photocatalytic property, low electronic band gap, and simple synthesis process.[27−29] The band gap of ZnO is 3.2 eV at room temperature. Therefore, the emission wavelength appropriate for gas sensing is around 387 nm, which is well matched to the designed LP's wavelength.[14] LPs
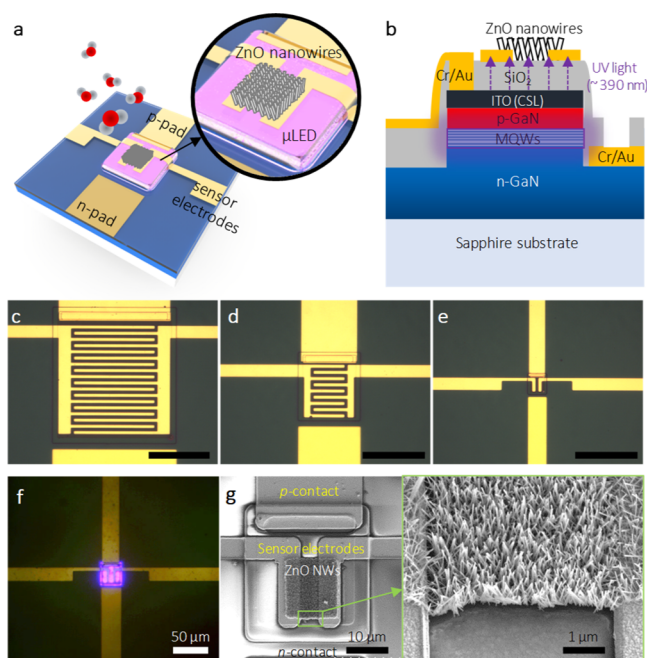

Figure 1. Schematic illustration of the proposed monolithic photoactivated gas sensors on a μLP: (a) top view and (b) cross-sectional view. Optical microscopic images of fabricated LPs are as follows: (c−e) 200×200 (200-LP), 100×100 (100-LP), and 30×30 (30-μLP) μm^2, respectively. Scale bars are 100 μm. (f) Optical microscopic image of a turned-on 30-μLP (forward bias = 5 V). (g) SEM images of synthesized zinc oxide (ZnO) nanowires on a prefabricated 30-μLP.

were fabricated through well-defined microfabrication processes.

Figure 1c−e shows optical microscope images of fabricated LPs with widths of 200, 100, and 30 μm, respectively, and Figure 1f shows the illumination from 30-μLP by applying forward bias of 5 V. Figure 1g shows the scanning electron microscopy (SEM) images of ZnO nanowires directly grown on top of the sensing electrodes through hydrothermal reaction. At first, as-synthesized ZnO nanowires covered the whole sensor chip. To define the sensing area, ZnO nanowires on the sensing electrodes were protected by the photoresist mask patterned via the standard photolithography method, and the other exposed nanowires were etched out with 3% nitric acid diluted in deionized (DI) water. As shown in Figure 1g, the average (standard deviation) of diameters and lengths of synthesized ZnO nanowires were 40.5 nm ($\pm$6.7 nm) and 349 nm ($\pm$114 nm), respectively. The detailed fabrication process is described in the overlap "Experimental Section" and in Figure S1 in the Supporting Information. Also, various SEM images of fabricated devices are provided in Figure S2 in the Supporting Information. As explained above, the combination of sensing nanomaterials and LP was carefully chosen to maximize the coupling efficiency. Figure S3 shows emitting spectrum of the fabricated LP and absorption spectrum of synthesized ZnO nanowires. The absorption band of ZnO nanowires well overlapped the emission spectrum of LP. Here, native defects in ZnO nanowires might contribute to broadening the absorbance spectrum beyond the intrinsic band gap of ZnO.[30] LEDs with much shorter emission wavelength ($\lambda_{peak} \ll$ 390 nm) may guarantee more definite photoactivation of ZnO nanowires, increasing the coupling efficiency between the LP and the sensing component.
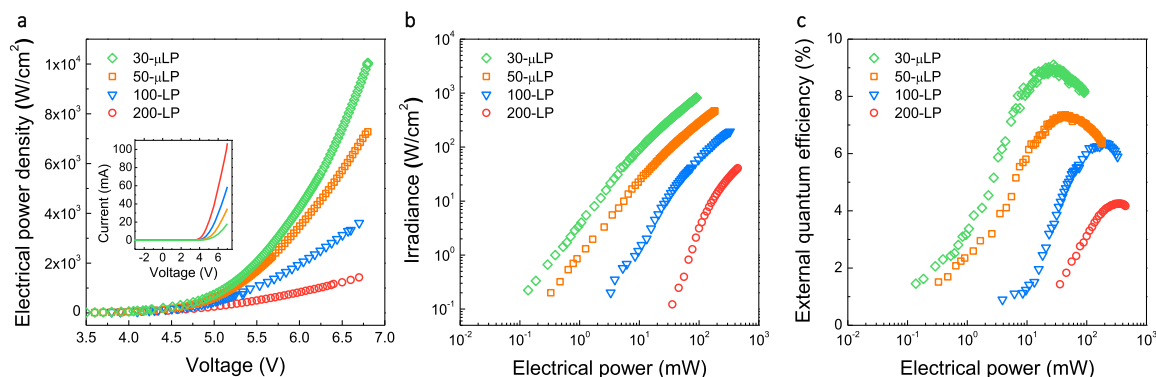
Figure 2. Performance of LPs with different sizes (30-μLP, 50-μLP, 100-LP, and 200-LP): (a) electrical power density depending on the applied forward bias from 3.5 to 6.7 V. (inset: $I-V$ curves) (b) irradiance, and (c) EQE depending on the input electrical power.

However, because the external quantum efficiency (EQE) of UV LEDs drastically decreases with increasing photon energy of UV LEDs, the actual energy efficiency with shorter wavelength of LED ($\lambda_{peak} \ll 390$ nm) can be lowered.[31−33] In addition, electrical insulation between the LED and the sensing component can be difficult under irradiation of high energy photons. These technical issues should be solved to utilize UV B or UV C LEDs in the integrated photoactivated gas sensor in the future.

The light-current−voltage ($L-I-V$) measurements were performed to characterize the electrical and the optical properties of fabricated LPs (Figure 2). In Figure 2a, the electrical power densities of various sized LPs (30-μLP, 50-μLP, 100-LP, and 200-LP) were obtained by measuring $I-V$ characteristics (inset graph in Figure 2a) with forward voltage ranging from 3.5 to 6.7 V. Turn-on voltage was measured around 4 V for all sized LPs. The $I-V$ characteristics showed a strong size-dependent behavior. The overall range of forward current was much lower at the smaller size of μLPs. On the other hand, the electrical power density was substantially increased as decreasing the size of the LP because of improved current spreading in small μLPs. From an equivalent circuit model of a lateral LED, the current density at the n-contact edge can be written as

$$J_n(L) = J_p \exp\left(-\frac{L}{L_s}\right) \tag{1}$$

where J_n and J_p are the current densities near n and p contact edges, respectively, and L is the lateral size of the LED.[34,35] In case of lateral LEDs, the current is laterally spread mainly through ITO and n-GaN layers. Therefore, the current spreading length (L_s), where the current density drops to $1/e$ ($\sim$0.37), is determined by the resistivity and thickness of each layer as

$$L_s = \sqrt{(\rho_c + \rho_p t_p)|\rho_n/t_n - \rho_{ITO}/t_{ITO}|^{-1}} \tag{2}$$

where ρ_c is the contact resistivity, ρ_p, ρ_n, and ρ_{ITO} are the resistivity, and t_p, t_n, and t_{ITO} are the thickness of p-GaN, n-GaN, and ITO layers, respectively. Although achieving perfect current spreading is possible at the critical condition $\rho_n/t_n = \rho_{ITO}/t_{ITO}$ (which means that L_s is infinite), the current spreading length is limited in the real situation. In general, carrier recombination mainly occurs near the p-contact, called as "current crowding" because the resistance of n-GaN is lower than that of ITO ($\rho_n/t_n \ll \rho_{ITO}/t_{ITO}$), and the carrier mobility

of p-GaN is nearly 1 order of magnitude lower than that of n-GaN.[36] As a result, smaller μLPs (30-μLP and 50-μLP) with small L/L_s show more effective current spreading and uniform carrier distribution than larger LPs (100-LP and 200-LP).

The irradiance (W/m^2) of various sized LPs was obtained by the electroluminescence measurement. Theoretically, the irradiance is determined by the electrical power density and the energy conversion efficiency of LED as follows

$$E_e \approx M_e = \frac{\Phi_e}{A} = \eta_{EQE}\frac{P_{electric}}{A} \tag{3}$$

where E_e and M_e are the irradiance and the radiant exitance of the LED in the radiometry, respectively, Φ_e is the total radiant flux, η_{EQE} is the EQE, $P_{electric}$ is the input electrical power, and A is the emission area of the LED. Because of the close proximity of the light source and the sensing material ($\sim$500 nm), the irradiance on the sensing material equals the radiant exitance from the LP.[21] As shown in Figure 2b, the smallest LP (i.e., 30-μLP) showed the highest irradiance ($\sim$820 W/cm^2 at 90 mW), which is nearly 430 times larger than the irradiance of the biggest LP (i.e., 200-LP) ($\sim$2.1 W/cm^2 at the same input power). This large enhancement of irradiance was contributed by the increased EQE and the electrical power density of μLPs. Figure 2c represents the EQE of various sized LPs according to the input electrical power. Overall EQE were increased as decreasing the size of LPs, and the maximum EQE of 30-μLP ($\sim$9.1%) was 2.2 times higher than that of the 200-LP ($\sim$4.2%). Interestingly, this size-dependent tendency of our UV LED is opposite to those of general visible LEDs. Generally, nonradiative recombination at the sidewall defects induced by dry-etching leads the degraded EQE of visible μLEDs.[25,37] However, EQE tendency of our UV LED can be explained by the effect of self-heating during LED operation. If the temperature of UV LED increases, carriers (i.e., electrons and holes) can thermally escape from the shallow energy level in the quantum wells to the surface state instead of radiative recombination (a schematic explanation is in Figure S4a in the Supporting Information).[38] The effective current spreading of small μLPs alleviates the current crowding and localized heating. Furthermore, large sidewall area per volume of μLPs leads to the effective heat dissipation and lower junction temperature.[39] Figure S4b in the Supporting Information shows peak wavelength shift under increasing current density. The negligible peak shift of small μLPs (30-μLP and 50-μLP) is the strong evidence of the low junction temperature, while the large red-shift is observed in bigger LPs (100-LP and 200-
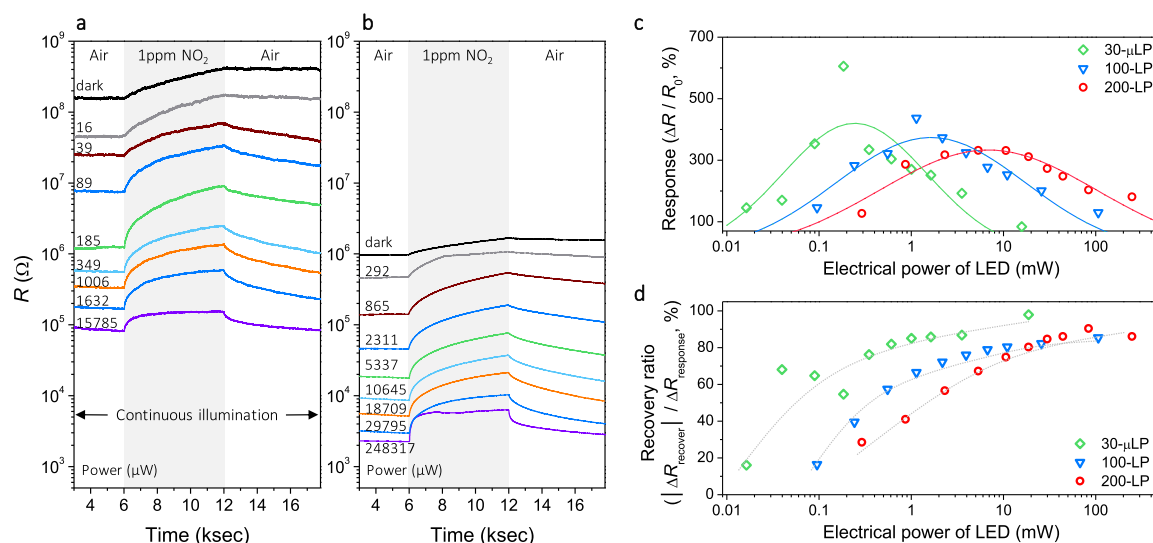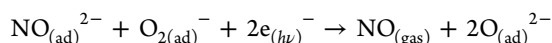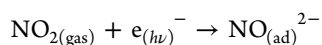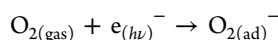
Figure 3. Responses of monolithic photoactivated gas sensors on (a) 30-μLP and (b) 200-LP to 1 ppm NO_2 gas under different input electrical powers. Summary of (c) normalized response [$(R - R_{air})/R_{air} \times 100$ (%)], and (d) recovery ratio [$|\Delta R_{recovery \, for \, 6ks}|/\Delta R_{response \, for \, 6ks} \times 100$ (%)] of 30-μLP, 100-LP, and 200-LP.

LP) because of the shrinkage of band gap energy by the localized heating. The performance of photoactivated gas sensor depends on the irradiance reaching the sensing material. Therefore, based on the improved energy efficiency, smaller μLP can produce similar effect on the gas sensing performance with much lower input power.

Gas sensing tests of fabricated sensors were conducted with nitrogen dioxide (NO_2) gas. NO_2 is the representative outdoor hazardous gas released from chemical plants and automobiles. The short-term recommended exposure limit of NO_2 is 1 ppm by National Institution for Occupational Safety and Health (NIOSH) guidelines.[40] The NO_2 sensing mechanism promoted by UV photoactivation can be explained by the following reactions

$$O_{2(gas)} + e_{(h\nu)}^{-} \rightarrow O_{2(ad)}^{-}$$

$$NO_{2(gas)} + e_{(h\nu)}^{-} \rightarrow NO_{(ad)}^{2-}$$

$$NO_{(ad)}^{2-} + O_{2(ad)}^{-} + 2e_{(h\nu)}^{-} \rightarrow NO_{(gas)} + 2O_{(ad)}^{2-}$$

where $e_{(h\nu)}^{-}$ is the photoelectron generated by UV irradiation.[41-43] These reaction mechanisms indicate that photoelectrons promote the adsorption of ionized oxygen species ($O_{2(ad)}^{-}$ or the form of O^{-}/O^{2-} by the spontaneous transition) and dissociation of NO_2 molecules at the surface of metal oxides. Because of surface depletion by electron transfer from metal oxides to surface oxygen, the resistance of n-type ZnO increases under NO_2 exposure. Figure 3a,b shows the responses of monolithic photoactivated gas sensors with different sizes (30-μLP and 200-LP) to 1 ppm NO_2 gas under increasing LED operating power. The base resistance of both sensors in air decreased as increasing the operating power of LED because of the generation of photoelectrons. The overall resistance of the ZnO nanowires on 30-μLP was higher than that of ZnO nanowires on 200-LP because the sensor on a smaller area has less electrical paths of ZnO nanowires between sensor electrodes (the gap between electrodes was consistent for all LP; 5 μm). The response of the sensor on 100-LP in the same experimental condition is presented in Figure S5 in the Supporting Information. We summarized the

normalized response [$(R - R_{air})/R_{air} \times 100$ (%)] and the recovery ratio [$|\Delta R_{recovery \, for \, 6ks}|/\Delta R_{response \, for \, 6ks} \times 100$ (%)] of the sensors on 30-μLP, 100-LP, and 200-LP, according to the applied LED power in Figure 3c,d. Normalized responses of each sensor basically showed bell-shaped tendencies. Prades et al. provided explanations of this bell-shaped tendency using a single SnO_2 nanowire and an UV LED.[44] They suggested physical models of relationship between the sensor response and irradiated photon flux and found that the optimal photon flux to maximize the sensing response is determined by the balance of surface densities of adsorbates (O_2 and NO_2) on the surface of metal oxides. In dark conditions ($\Phi_e \rightarrow 0$), inflowing NO_2 molecules cannot replace pre-adsorbed oxygen ions because of the inactive surface (small $R_{NO_2} - R_{air}$), while adsorbates are totally desorbed in high-flux conditions ($\Phi_e \rightarrow \infty$).[45] In the same manner, our sensor also had optimal LED operating power maximizing the sensor response. Data points were well fitted to the log–normal distribution function $\left[f(x) = \frac{1}{x\sigma\sqrt{2\pi}} \exp\left(-\frac{(\ln x - \mu)^2}{2\sigma^2}\right) \right]$. Peak modes [defined as $\exp(\mu - \sigma^2)$] of each curve decreased with reducing the size (peak mode = 6800, 1600, and 244 μW at 200-LP, 100-LP, and 30-μLP, respectively). Furthermore, they showed improvement of the peak response at the optimal power with the size reduction of LP (334, 436, and 605% for 200-LP, 100-LP, and 30-μLP, respectively). These improvements by the size reduction can be explained by the enhanced current spreading of μLPs. From eq 1, $J_n/J_p \approx 1$ is ideally desired for uniform light power density (W/cm^2) across the emitting area. However, J_n/J_p drops as the lateral length (L) of the LED increases because of increasing lateral series resistance. It means that poor current spreading induces inhomogeneous light power density across the emitting area.[46] The lower average irradiance of the 200-LP shown in Figure 2b and optical microscopy images of illuminating LPs in Figure S6 in the Supporting Information support this fact. Therefore, the sensing materials on the less irradiating region (dark spot) can give less contribution to gas sensing, similar with the "cold zone" or "dead zone" of the SMO-based gas sensor on the
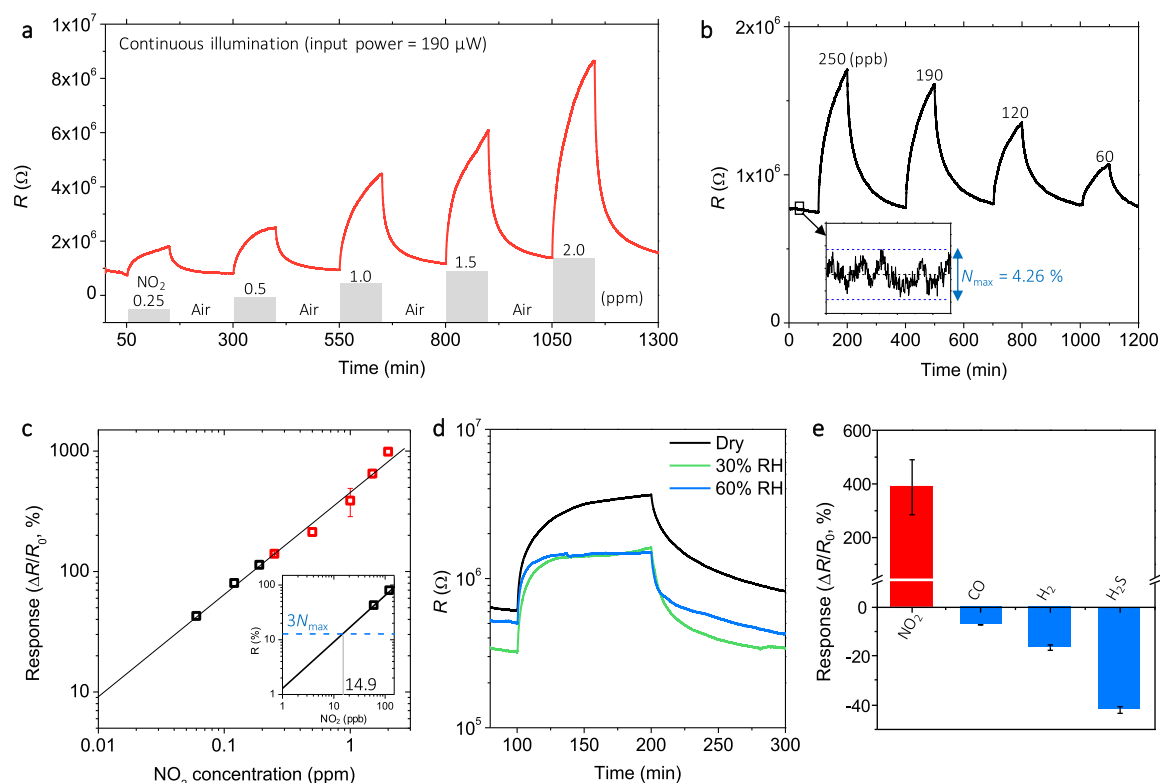
Figure 4. Nitrogen dioxide (NO_2) sensing performance of the photoactivated gas sensor on 30-μLP. Whole tests were conducted under an operating power of ~190 μW: dynamic response to (a) 0.25−2 ppm and (b) 60−250 ppb NO_2 gas. The inset graph shows the noise level of the measurement. (c) Calibration graph of normalized sensor response [$(R − R_{air})/R_{air} \times 100$ (%)] to NO_2 concentrations, and lower LOD is ~14.9 ppb. (d) Humidity interference test under 30 and 60% of relative humidity (RH) and 1 ppm NO_2 gas. (e) Gas selectivity test to 1 ppm NO_2, 160 ppm carbon monoxide (CO), 3.2% hydrogen (H_2), and 10 ppm hydrogen sulfide (H_2S).

heating platforms.[47] Thus, if the portion of these "dead zones" in the overall sensing resistance become larger as increasing the LED size, normalized sensor responses will become lower. Complete recovery of the sensor signal is also important for the repeatability of the gas sensor. Figure 3d shows the recovery ratio, defined as the ratio of resistance change during recovery to response [$|\Delta R_{recovery\,for\,6ks}|/\Delta R_{response\,for\,6ks} \times 100$ (%)] of the sensors on 30-μLP, 100-LP, and 200-LP. For the tests, response and recovery times were set as 6000 s each. During the response and recovery, the recovery ratio increased as the LED operating power (which is proportional to irradiance) increased. It is because the rate of photo-adsorption and photo-desorption is promoted by sufficient photon flux, and the surface state reaches the equilibrium much faster.[44] In the present state, slow response and recovery may cause limited practical applications. Surface modification of sensing materials with catalytic materials or the heterojunction structure of multiple SMOs can be adopted for improving the response and recovery speeds through future investigation.

We performed further NO_2 gas tests with our smallest sensor device, 30-μLP. Whole tests were conducted near its optimal operating power at the experimental peak point (~190 μW). Figure 4a shows the dynamic response of the sensor to NO_2 gas with concentrations ranging from 0.25 to 2 ppm. The result shows clear response and recovery over the wide concentration range. In order to investigate the lower LOD, the sensor was exposed to the lower concentration range of NO_2 (60−250 ppb), as shown in Figure 4b. A value of 60 ppb was the lowest concentration we could generate by our testing facility. The sensor shows a clear response even to the 60 ppb NO_2. For

more accurate evaluation, the noise level of measurement was calculated at the baseline signal (see the inset graph in Figure 4b). The maximum noise level (N_{max}) was 4.26%, and the LOD can be determined at the point where the signal is three times larger than the maximum noise level ($3N_{max}$).[48] Figure 4c is the calibration graph of the normalized sensor response [$(R − R_{air})/R_{air} \times 100$ (%)] to NO_2 concentrations. The sensor response was well fitted to a linear function at the log−log scale plot [$\log(\Delta R/R_0) = 0.8485 \times \log(P) + 2.657$, $r^2 = 0.99$, where P is the NO_2 concentration (ppm)]. The extrapolated line met $3N_{max}$ (=12.78%) at NO_2 concentration = 14.9 ppb. Therefore, we concluded that our photo-activated sensor on the 30-μLP is able to detect ultra-low concentration (14.9 ppb) of NO_2. In Table S1, the sensing performance of the monolithic photoactivated gas sensor on 30-μLP was compared with other reported gas sensors with various activation sources such as micro/nano heating platforms, external light sources, and embedded LEDs. Our sensor shows a record of low power consumption, as well as comparable sensing performance compared with previous works.

To investigate the influence of humidity on the sensor performance, the response to 1 ppm NO_2 gas under different RH (0, 30, and 60 % RH) conditions were measured, as shown in Figure 4d. In the humid condition, the hydroxyl group (−OH) dissociated from water molecules adsorbed on the surface of the metal oxide and hindered the adsorption sites of oxygen and NO_2. Therefore, the normalized sensor response was decreased, as increasing the RH [$\Delta R/R_{air} \times 100$ (%) = 499, 401, and 197% under 0, 30, and 60 % RH, respectively], and it can be generally seen at SMO gas sensors. Despite the

reduction of responses by the humidity effect, the compensation of the sensor signal from humidity interference will be possible with real-time humidity monitoring, because the sensor signal to NO_2 gas is distinct even under the humid condition.

Figure 4e shows the response $[\Delta R/R_{air} \times 100 \ (\%)]$ of the sensor for different types of gases such as carbon monoxide (CO), hydrogen (H_2), and hydrogen sulfide (H_2S). These reducing gases provide electrons to SMOs when they adsorb on the surface of SMOs. Therefore, they make the resistance of n-type ZnO decrease. The concentrations of each tested gas were the maximum concentration that our experimental setup could generate (160, 3.2%, and 10 ppm of CO, H_2, and H_2S respectively), and all are close to the permissible exposure limit or lower explosive limit by the safety guideline.[40] As shown in Figure 4e, the sensor showed the greatest response to the NO_2 gas $[\Delta R/R_{air} \times 100 \ (\%) = 388\%]$. Other reducing gases showed reverse response ($\Delta R/R_{air} < 0$) and relatively smaller responses ($\Delta R/R_{air} = -7.2$, -16.6, and -42% for 160 ppm CO, 3.2% H_2, and 10 ppm H_2S, respectively). Therefore, the developed sensor can be utilized for selective detection of NO_2 gas.

CONCLUSIONS

In conclusion, an ultra-low power photoactivated gas sensor, monolithically integrated onto a miniaturized μLP was introduced. The 30 μm-sized μLED platform (30-μLP) achieved the superior energy efficiency because of proximity ($\sim$500 nm) with sensing materials and the intrinsic high irradiance and the EQE ($\sim$9%) of μLPs. High irradiance and EQE of the μLP was mainly due to the improved current spreading that can suppress the undesired current crowding near the p-contact. Furthermore, ZnO nanowires integrated on 30-μLP showed superior sensing performance ($\Delta R/R_{air} = 605\%$ to 1 ppm NO_2) compared to the sensor on 200-LP ($\Delta R/R_{air} = 334\%$ to 1 ppm NO_2) because effective current spreading of μLP allowed uniform emission across the emitting area. The sensor on 30-μLP showed ultralow LOD ($\sim$15 ppb NO_2), humidity robustness, and high NO_2 selectivity to other interfering gases under low operating power ($\sim$190 μW). All sensing tests were conducted at room temperature so that the sensor can avoid undesired degradation because of thermal aging. Excellent gas sensing performance and ultralow operating power promise applications on the battery-driven IoT devices. Finally, this work provides a new route of emerging μLED technology as chemical sensors for future healthcare, personalized environmental monitoring, and smart factory applications.

EXPERIMENTAL SECTION

Fabrication of LPs. The whole fabrication process is graphically described in Figure S1 in the Supporting Information. A stack of high-purity n-type (3 μm) GaN, InGaN/GaN multi-quantum well (MQW) layer (50 nm), and p-type GaN (200 nm) layer was epitaxially grown on a sapphire substrate through a metal−organic CVD (conducted by GenUV, South Korea). GaN layers were patterned with photoresist (AZnlof 2035, MicroChemicals, Germany) and vertically etched via inductively coupled plasma-reactive ion etching (ICP-RIE) for 2 min to formulate mesa structures of LPs. ICP-RIE was conducted in the Cl (60 sccm) and Ar (20 sccm) atmosphere, maintaining the 10 mtorr pressure with a radio frequency power of 250 W (plasma power = 700 W). Here, the widths of square LEDs were designed to 30, 50, 100, and 200 μm. On top of the mesa structure, 200 nm thick ITO and p−n contact metals [10 nm chromium (Cr) and 200 nm gold (Au)]

were sequentially patterned by UV photolithography and electron-beam (e-beam) evaporation. Here, the ITO layer roles as a current spreading layer. As-deposited ITO was heat-treated at 750 °C through rapid thermal annealing process for the enhanced optical transparency and electrical conductivity. Silicon dioxide (SiO_2) insulation layer (500 nm thick) was deposited using plasma-enhanced CVD process and vertically etched via RIE ($CF_4/O_2 = 9:1$, 150 mtorr, 50 W) for opening contact pads. Finally, sensor electrodes (10 nm Cr/200 nm Au) were patterned on an insulation layer by UV photolithography and e-beam evaporation.

Growth of Zinc Oxide Nanowires on the Fabricated LPs. Zinc oxide (ZnO) nanowires were synthesized by the well-established hydrothermal reaction.[49−52] Prior to the synthesis, a thin layer of ZnO nanoparticles was deposited using the sputtering system (5 mtorr of argon atmosphere, 150 W, 3 min) on fabricated LPs. A precursor solution was prepared by mixing 25 mM zinc nitrate hexahydrate, 25 mM hexamethylenetetramine, and 6 mM polyethyleneimine in DI water. Prefabricated LPs were immersed into the precursor solution and heated up to 95 °C for 2 h in a convection oven. Then, ZnO nanowires grew on the whole surface of the device. In order to define the sensing area, ZnO nanowires grown on the sensor electrodes were covered with a 3 μm thick photoresist (AZ5214, MicroChemicals, Germany). Exposed ZnO nanowires out of the sensing area were removed in an acidic etchant (3% nitric acid diluted in DI water) for 5 s. Finally, photoresist masks were removed by acetone, and the device was washed with DI water.

Characterization of the Fabricated Devices. The fabricated sensor devices were visually observed by field emission scanning electron microscopy [FE-SEM (SU8230), Hitachi, Japan]. In order to analyze the photon absorbance of ZnO nanowires, they were synthesized on a transparent quartz substrate, and an absorbance spectrum was measured using the ultraviolet−visible (UV−vis) spectrophotometer (Lambda 1050, PerkinElmer, USA) with an integrating sphere. Optical and electrical properties of LPs were obtained using the $L-I-V$ measurement system (OPI 160, WITHLIGHT, Korea) with an integrating sphere and a source meter (Keithley 2400, USA).

Gas Sensing Test. The sensor devices were mounted on a custom-made testing chamber and connected to current sourcemeters (Keithley 2400 and 2635b, USA) for applying forward bias on a μLPs and measuring the sensing resistance, respectively. Forward bias applied on the LP was swept from 3.2 to 6 V for each gas test to find the optimal operating power. Gas was supplied to the sensor device, and the concentration of NO_2 gas was adjusted by controlling the flow rates of NO_2 gas and dry air [that is, $\sim$0% RH] with mass flow controllers. For the humidity interference test, RH was controlled to 30 and 60 % RH by changing the proportion of the dry air and the humid air generated by a water-bubbling system. Carbon monoxide (CO), hydrogen (H_2), and hydrogen sulfide (H_2S), which are indoor/outdoor hazardous gases, were utilized for the gas selectivity test.

ASSOCIATED CONTENT

Ⓢ Supporting Information

The Supporting Information is available free of charge at https://pubs.acs.org/doi/10.1021/acssensors.9b02487.

Detailed fabrication process, SEM images of fabricated devices, electroluminescence spectrum of fabricated LED, absorbance spectrum of hydrothermally grown zinc oxide nanowires, simplified band model of MQWs in the GaN-LED, peak wavelength shift of LEDs, response of the gas sensor on the 100-LP, comparison of emission uniformity according to the size of LED, and summary of gas sensors based on various activation sources (PDF)

AUTHOR INFORMATION

Corresponding Authors

Yong-Hoon Cho − *Korea Advanced Institute of Science and Technology (KAIST), Daejeon, Republic of Korea;* orcid.org/0000-0002-7701-8562; Email: yhc@kaist.ac.kr

Inkyu Park − *Korea Advanced Institute of Science and Technology (KAIST), Daejeon, Republic of Korea;* orcid.org/0000-0001-5761-7739; Email: inkyu@kaist.ac.kr

Other Authors

Incheol Cho − *Korea Advanced Institute of Science and Technology (KAIST), Daejeon, Republic of Korea*

Young Chul Sim − *Korea Advanced Institute of Science and Technology (KAIST), Daejeon, Republic of Korea*

Minkyu Cho − *Korea Advanced Institute of Science and Technology (KAIST), Daejeon, Republic of Korea;* orcid.org/0000-0002-0006-2063

Complete contact information is available at:
https://pubs.acs.org/10.1021/acssensors.9b02487

Author Contributions

I.C., Y.C.S., and M.C. have contributed equally. I.C. and Y.C.S. planned and conducted the experiments and wrote the paper. M.C. conceived the original ideas. Y.-H.C. and I.P. supervised the project. All authors have given approval to the final version of the manuscript.

Notes

The authors declare no competing financial interest.

REFERENCES

(1) Wang, C.; Yin, L.; Zhang, L.; Xiang, D.; Gao, R. Metal oxide gas sensors: sensitivity and influencing factors. *Sensors* **2010**, *10*, 2088−2106.

(2) Choi, K. J.; Jang, H. W. One-dimensional oxide nanostructures as gas-sensing materials: review and issues. *Sensors* **2010**, *10*, 4083−4099.

(3) Kim, H.-J.; Lee, J.-H. Highly sensitive and selective gas sensors using p-type oxide semiconductors: Overview. *Sens. Actuators, B* **2014**, *192*, 607−627.

(4) Bhattacharyya, P. Technological journey towards reliable microheater development for MEMS gas sensors: A review. *IEEE Trans. Device Mater. Reliab.* **2014**, *14*, 589−599.

(5) Zhou, Q.; Sussman, A.; Chang, J.; Dong, J.; Zettl, A.; Mickelson, W. Fast response integrated MEMS microheaters for ultra low power gas detection. *Sens. Actuators, A* **2015**, *223*, 67−75.

(6) Kang, K.; Yang, D.; Park, J.; Kim, S.; Cho, I.; Yang, H.-H.; Cho, M.; Mousavi, S.; Choi, K. H.; Park, I. Micropatterning of metal oxide nanofibers by electrohydrodynamic (EHD) printing towards highly integrated and multiplexed gas sensor applications. *Sens. Actuators, B* **2017**, *250*, 574−583.

(7) Cho, I.; Kang, K.; Yang, D.; Yun, J.; Park, I. Localized liquid-phase synthesis of porous SnO_2 nanotubes on MEMS platform for low-power, high performance gas sensors. *ACS Appl. Mater. Interfaces* **2017**, *9*, 27111−27119.

(8) Choi, K.-W.; Lee, J.-S.; Seo, M.-H.; Jo, M.-S.; Yoo, J.-Y.; Sim, G. S.; Yoon, J.-B. Batch-fabricated CO gas sensor in large-area (8-inch) with sub-10 mW power operation. *Sens. Actuators, B* **2019**, *289*, 153−159.

(9) Rao, A.; Long, H.; Harley-Trochimczyk, A.; Pham, T.; Zettl, A.; Carraro, C.; Maboudian, R. In situ localized growth of ordered metal oxide hollow sphere array on microheater platform for sensitive, ultra-fast gas sensing. *ACS Appl. Mater. Interfaces* **2017**, *9*, 2634−2641.

(10) Long, H.; Harley-Trochimczyk, A.; He, T.; Pham, T.; Tang, Z.; Shi, T.; Zettl, A.; Mickelson, W.; Carraro, C.; Maboudian, R. In situ localized growth of porous tin oxide films on low power microheater platform for low temperature CO detection. *ACS Sens.* **2016**, *1*, 339−343.

(11) Lim, Y.; Lee, S.; Kwon, Y. M.; Baik, J. M.; Shin, H. In Gas sensor based on a metal oxide nanowire forest built on a suspended carbon nano-heater. *31th IEEE International Conference on Micro Electro Mechanical Systems*; IEEE, 2018; pp 905−907.

(12) Meng, G.; Zhuge, F.; Nagashima, K.; Nakao, A.; Kanai, M.; He, Y.; Boudot, M.; Takahashi, T.; Uchida, K.; Yanagida, T. Nanoscale thermal management of single SnO_2 nanowire: pico-Joule energy consumed molecule sensor. *ACS Sens.* **2016**, *1*, 997−1002.

(13) Espid, E.; Taghipour, F. Development of highly sensitive ZnO/In_2O_3 composite gas sensor activated by UV-LED. *Sens. Actuators, B* **2017**, *241*, 828−839.

(14) Espid, E.; Taghipour, F. UV-LED photo-activated chemical gas sensors: A review. *Crit. Rev. Solid State Mater. Sci.* **2017**, *42*, 416−432.

(15) Saura, J. Gas-sensing properties of SnO_2 pyrolytic films subjected to ultrviolet radiation. *Sens. Actuators, B* **1994**, *17*, 211−214.

(16) Cho, M.; Park, I. Recent trends of light-enhanced metal oxide gas sensors. *J. Sens. Sci. Technol.* **2016**, *25*, 103−109.

(17) Gong, B.; Shi, T.; Zhu, W.; Liao, G.; Li, X.; Huang, J.; Zhou, T.; Tang, Z. UV irradiation-assisted ethanol detection operated by the gas sensor based on ZnO nanowires/optical fiber hybrid structure. *Sens. Actuators, B* **2017**, *245*, 821−827.

(18) Wang, C. Y.; Cimalla, V.; Kups, T.; Röhlig, C.-C.; Stauden, T.; Ambacher, O.; Kunzer, M.; Passow, T.; Schirmacher, W.; Pletschen, W.; Köhler, K.; Wagner, J. Integration of In_2O_3 nanoparticle based ozone sensors with GaInN/GaN light emitting diodes. *Appl. Phys. Lett.* **2007**, *91*, 103509.

(19) Hsu, C.-L.; Chang, L.-F.; Hsueh, T.-J. Light-activated humidity and gas sensing by ZnO nanowires grown on LED at room temperature. *Sens. Actuators, B* **2017**, *249*, 265−277.

(20) Casals, O.; Markiewicz, N.; Fabrega, C.; Gràcia, I.; Cané, C.; Wasisto, H. S.; Waag, A.; Prades, J. D. A Parts Per Billion (ppb) Sensor for NO_2 with Microwatt (μW) Power Requirements Based on Micro Light Plates. *ACS Sens.* **2019**, *4*, 822−826.

(21) Markiewicz, N.; Casals, O.; Fabrega, C.; Gràcia, I.; Cané, C.; Wasisto, H. S.; Waag, A.; Prades, J. D. Micro light plates for low-power photoactivated (gas) sensors. *Appl. Phys. Lett.* **2019**, *114*, 053508.

(22) Jiang, H. X.; Lin, J. Y. Nitride micro-LEDs and beyond - a decade progress review. *Opt. Express* **2013**, *21*, A475−A484.

(23) Wu, T.; Sher, C.-W.; Lin, Y.; Lee, C.-F.; Liang, S.; Lu, Y.; Huang Chen, S.-W.; Guo, W.; Kuo, H.-C.; Chen, Z. Mini-LED and micro-LED: promising candidates for the next generation display technology. *Appl. Sci.* **2018**, *8*, 1557.

(24) Tian, P.; McKendry, J. J. D.; Gong, Z.; Guilhabert, B.; Watson, I. M.; Gu, E.; Chen, Z.; Zhang, G.; Dawson, M. D. Size-dependent efficiency and efficiency droop of blue InGaN micro-light emitting diodes. *Appl. Phys. Lett.* **2012**, *101*, 231110.

(25) Olivier, F.; Tirano, S.; Dupré, L.; Aventurier, B.; Largeron, C.; Templier, F. Influence of size-reduction on the performances of GaN-

based micro-LEDs for display application. *J. Lumin.* **2017**, *191*, 112−116.

(26) Ploch, N. L.; Rodriguez, H.; Stolmacker, C.; Hoppe, M.; Lapeyrade, M.; Stellmach, J.; Mehnke, F.; Wernicke, T.; Knauer, A.; Kueller, V.; Weyers, M.; Einfeldt, S.; Kneissl, M. Effective Thermal Management in Ultraviolet Light-Emitting Diodes With Micro-LED Arrays. *IEEE Trans. Electron Devices* **2013**, *60*, 782−786.

(27) Wan, Q.; Li, Q. H.; Chen, Y. J.; Wang, T. H.; He, X. L.; Li, J. P.; Lin, C. L. Fabrication and ethanol sensing characteristics of ZnO nanowire gas sensors. *Appl. Phys. Lett.* **2004**, *84*, 3654−3656.

(28) Sivalingam, Y.; Martinelli, E.; Catini, A.; Magna, G.; Pomarico, G.; Basoli, F.; Paolesse, R.; Di Natale, C. Gas-sensitive photo-conductivity of porphyrin-functionalized ZnO nanorods. *J. Phys. Chem. C* **2012**, *116*, 9151−9157.

(29) Peng, L.; Zhai, J.; Wang, D.; Zhang, Y.; Wang, P.; Zhao, Q.; Xie, T. Size-and photoelectric characteristics-dependent formaldehyde sensitivity of ZnO irradiated with UV light. *Sens. Actuators, B* **2010**, *148*, 66−73.

(30) Schmidt-Mende, L.; MacManus-Driscoll, J. L. ZnO − nanostructures, defects, and devices. *Mater. Today* **2007**, *10*, 40−48.

(31) Nagasawa, Y.; Hirano, A. A review of AlGaN-based deep-ultraviolet light-emitting diodes on sapphire. *Appl. Sci.* **2018**, *8*, 1264.

(32) Kneissl, M.; Kolbe, T.; Chua, C.; Kueller, V.; Lobo, N.; Stellmach, J.; Knauer, A.; Rodriguez, H.; Einfeldt, S.; Yang, Z.; Johnson, N. M.; Weyers, M. Advances in group III-nitride-based deep UV light-emitting diode technology. *Semicond. Sci. Technol.* **2010**, *26*, 014036.

(33) Muramoto, Y.; Kimura, M.; Nouda, S. Development and future of ultraviolet light-emitting diodes: UV-LED will replace the UV lamp. *Semicond. Sci. Technol.* **2014**, *29*, 084004.

(34) Kim, H.; Park, S.-J.; Hwang, H.; Park, N.-M. Lateral current transport path, a model for GaN-based light-emitting diodes: Applications to practical device designs. *Appl. Phys. Lett.* **2002**, *81*, 1326−1328.

(35) Guo, X.; Schubert, E. F. Current crowding and optical saturation effects in GaInN/GaN light-emitting diodes grown on insulating substrates. *Appl. Phys. Lett.* **2001**, *78*, 3337−3339.

(36) Chen, H.-S.; Yeh, D.-M.; Lu, C.-F.; Huang, C.-F.; Lu, Y.-C.; Chen, C.-Y.; Huang, J.-J.; Yang, C. C. Mesa-size-dependent color contrast in flip-chip blue/green two-color In GaN/GaN multi-quantum-well micro-light-emitting diodes. *Appl. Phys. Lett.* **2006**, *89*, 093501.

(37) Konoplev, S. S.; Bulashevich, K. A.; Karpov, S. Y. From large-size to micro-LEDs: scaling trends revealed by modeling. *Phys. Status Solidi A* **2018**, *215*, 1700508.

(38) Mukai, T.; Nakamura, S. Ultraviolet InGaN and GaN single-quantum-well-structure light-emitting diodes grown on epitaxially laterally overgrown GaN substrates. *Jpn. J. Appl. Phys.* **1999**, *38*, 5735.

(39) Gong, Z.; Jin, S.; Chen, Y.; McKendry, J.; Massoubre, D.; Watson, I. M.; Gu, E.; Dawson, M. D. Size-dependent light output, spectral shift, and self-heating of 400 nm InGaN light-emitting diodes. *J. Appl. Phys.* **2010**, *107*, 013103.

(40) Occupational Safety and Health Administration (OSHA). *Toxic and Hazardous Substances 1915.1000*; Occupational Safety and Health Administration: Washington, D.C., USA, 2017.

(41) Wagner, T.; Kohl, C.-D.; Morandi, S.; Malagù, C.; Donato, N.; Latino, M.; Neri, G.; Tiemann, M. Photoreduction of mesoporous In₂O₃: mechanistic model and utility in gas sensing. *Chem.—Eur. J.* **2012**, *18*, 8216−8223.

(42) An, S.; Park, S.; Mun, Y.; Lee, C. UV enhanced NO₂ sensing properties of Pt functionalized Ga₂O₃ nanorods. *Bull. Korean Chem. Soc.* **2013**, *34*, 1632−1636.

(43) Karaduman, I.; Yıldız, D. E.; Sincar, M. M.; Acar, S. UV light activated gas sensor for NO₂ detection. *Mater. Sci. Semicond. Process.* **2014**, *28*, 43−47.

(44) Prades, J. D.; Jimenez-Diaz, R.; Manzanares, M.; Hernandez-Ramirez, F.; Cirera, A.; Romano-Rodriguez, A.; Mathur, S.; Morante, J. R. A model for the response towards oxidizing gases of photoactivated sensors based on individual SnO₂ nanowires. *Phys. Chem. Chem. Phys.* **2009**, *11*, 10881−10889.

(45) Prades, J. D.; Jimenez-Diaz, R.; Hernandez-Ramirez, F.; Barth, S.; Cirera, A.; Romano-Rodriguez, A.; Mathur, S.; Morante, J. R. Equivalence between thermal and room temperature UV light-modulated responses of gas sensors based on individual SnO₂ nanowires. *Sens. Actuators, B* **2009**, *140*, 337−341.

(46) Hwang, D.; Mughal, A.; Pynn, C. D.; Nakamura, S.; DenBaars, S. P. Sustained high external quantum efficiency in ultrasmall blue III−nitride micro-LEDs. *Appl. Phys. Express* **2017**, *10*, 032101.

(47) Peterson, P.; Aujla, A.; Grant, K.; Brundle, A.; Thompson, M.; Vande Hey, J.; Leigh, R. Practical use of metal oxide semiconductor gas sensors for measuring nitrogen dioxide and ozone in urban environments. *Sensors* **2017**, *17*, 1653.

(48) Shrivastava, A.; Gupta, V. Methods for the determination of limit of detection and limit of quantitation of the analytical methods. *Chron. Young Sci.* **2011**, *2*, 21−25.

(49) Greene, L. E.; Law, M.; Tan, D. H.; Montano, M.; Goldberger, J.; Somorjai, G.; Yang, P. General route to vertical ZnO nanowire arrays using textured ZnO seeds. *Nano Lett.* **2005**, *5*, 1231−1236.

(50) Yang, D.; Kim, D.; Ko, S. H.; Pisano, A. P.; Li, Z.; Park, I. Focused energy field method for the localized synthesis and direct integration of 1D nanomaterials on microelectronic devices. *Adv. Mater.* **2015**, *27*, 1207−1215.

(51) Kim, D.; Yang, D.; Kang, K.; Lim, M. A.; Li, Z.; Park, C.-O.; Park, I. In-situ integration and surface modification of functional nanomaterials by localized hydrothermal reaction for integrated and high performance chemical sensors. *Sens. Actuators, B* **2016**, *226*, 579−588.

(52) Jin, C. Y.; Li, Z.; Williams, R. S.; Lee, K.-C.; Park, I. Localized temperature and chemical reaction control in nanoscale space by nanowire array. *Nano Lett.* **2011**, *11*, 4818−4825.